ELSEVIER

Inhibition of vascular endothelial growth factor in young adult mice causes low bone blood flow and bone strength with no effect on bone mass in trabecular regions

N.E. Lane[a],[*], J.S. Nyman[b], S. Uppuganti[b], A.J. Chaudhari[c], J.I. Aguirre[d], K. Shidara[a], X.P. Liu[a], W. Yao[a], D.B. Kimmel[d]

[a] Center for Musculoskeletal Health, University of California at Davis Medical Center, Sacramento, CA 95817, USA
[b] Department of Orthopaedic Surgery and Rehabilitation, Vanderbilt University Medical Center, Nashville, TN 37232, USA
[c] Center for Molecular and Genomic Imaging, Department of Radiology, University of California at Davis, Davis, CA 95616, USA
[d] Department of Physiological Sciences, University of Florida, Gainesville, FL 32610, USA

A R T I C L E   I N F O

A B S T R A C T

Objective: To determine the effect of an antibody to vascular endothelial growth factor (VEGF) on bone blood flow, bone strength, and bone mass in the young adult mouse.

Methods: Ten-week-old male BALB/cJ mice were body weight-randomized into either a rodent anti-VEGF monoclonal antibody (anti-VEGF, B20-4.1.1; 5 mg/kg $2 \times$/wk.; n = 12) group or a vehicle (VEH; n = 12) group. After 42 days, mice were evaluated for bone blood flow at the distal femur by ^{18}F-NaF-PET/CT and then necropsied. Samples from trabecular and cortical bone regions were evaluated for bone strength by mechanical testing, bone mass by peripheral quantitative computed tomography (pQCT), and micoarchitecture (MicroCT). Hydration of the whole femur was studied by proton nuclear magnetic resonance relaxometry (^{1}H NMR).

Results: Distal femur blood flow was 43% lower in anti-VEGF mice than in VEH mice (p = 0.009). Ultimate load in the lumbar vertebral body was 25% lower in anti-VEGF than in VEH mice (p = 0.013). Bone mineral density (BMD) in the trabecular region of the proximal humeral metaphysis by pQCT, and bone volume fraction and volumetric BMD by MicroCT were the same in the two groups. Volume fraction of bound water (BW) of the whole femur was 14% lower in anti-VEGF than in VEH mice (p = 0.003). Finally, BW, but not cortical tissue mineral density, helped section modulus explain the variance in the ultimate moment experienced by the femur in three-point bending.

Conclusion: Anti-VEGF caused low bone blood flow and bone strength in trabecular bone regions without influencing BMD and microarchitecture. Low bone strength was also associated with low bone hydration. These data suggest that bone blood flow is a novel bone property that affects bone quality.

1. Introduction

Non-invasive assessment of fracture risk in humans involves measuring a series of bone properties that contribute to bone strength. DXA-based areal bone mineral density (BMD) of the spine and hip, a well-established endpoint that evaluates bone mass, has set a solid standard for evaluating prospective fracture risk in individuals (Kanis et al., 1994; Kanis and WHO Study Group, 1994). However, three independent lines of reasoning support the idea that by itself, BMD is insufficient to completely integrate all aspects of bone fragility. First, a history of fragility fracture at the spine or hip is a better predictor of future fracture than BMD (Ross et al., 1993). Second, anti-resorptive

therapy with a nitrogen-containing bisphosphonate (N-BP) or a RANK Ligand antibody, that increases spine BMD ~6–10% and hip BMD ~3–4% after three years, is far more effective in reducing fracture risk at the spine (by ~70%) and at the hip (by ~50%), than the BMD increases predict (Cummings et al., 1998; Harris et al., 1999; Delmas and Seeman, 2004; Cummings et al., 2002). Third, glucocorticoid (GC)-treated, diabetic, and hyperhomocysteinemic patients have higher fracture risk than is predicted by their BMD (Van Staa et al., 2003; Balasubramanian et al., 2018; Saag et al., 2009; Weinstein et al., 2010; Sellmeyer et al., 2016; Rubin, 2017; Behera et al., 2017; Blouin et al., 2009). This BMD/fracture risk gap has led to the study of bone quality as a bone mass-independent contributor to fracture risk (Fonseca et al.,

2014). Bone properties that may influence fracture risk independent of bone mass can be assessed by various non-invasive imaging techniques (bone geometry, trabecular microarchitecture, and cortical microstructure) (Manhard et al., 2017), a minimally invasive indentation method (Chang et al., 2018); serum biomarkers of bone turnover, collagen cross-linking, and protein glycation (Garnero, 2012); and analysis of bone biopsies (bone matrix composition, collagen fiber orientation, and degree of bone mineralization (Roschger et al., 2014).

Since vascular homeostasis is critical to healthy bone, one might hypothesize that bone blood flow is another such bone property (Weinstein et al., 2010; Fonseca et al., 2014). Under poor local perfusion or ischemic conditions, new blood vessels form to restore normal oxygen saturation or, in the case of bone, an adequate state of hypoxia (4% O_2). In healthy tissue, growth factors (e.g., fibroblast growth factors (FGFs), insulin-like growth factors (IGFs), hepatocyte growth factor (HGF), and platelet-derived growth factor (PDGF) act through paracrine or autocrine mechanisms to stimulate production of vascular endothelial growth factor (VEGF), which both maintains existing blood vessels and stimulates sprouting of new blood vessels (Senger, 2010; Murakami, 2012; Murakami and Simons, 2009; Maurea et al., 2016; Hu and Olsen, 2016a). New blood vessel formation in bone tissue is critical for vascular maintenance, healing bone defects, and even bone remodeling itself (Hu and Olsen, 2016a; Hirche et al., 2017), as after new blood vessels form, osteoclasts and osteoblasts are recruited (Hu and Olsen, 2016b; Tabbaa et al., 2014). When that vascularization is impeded, blood perfusion and formation of collateral circulation slows (Murakami, 2012; Liu et al., 2014). When juvenile male rats were treated with a bone anabolic dose of PTH or PTH combined with a rodent anti-VEGF antibody (anti-VEGF) for six weeks, PTH + anti-VEGF rats had 4% lower BMD, but 13% lower maximum load and 37% lower bone toughness in the femoral diaphysis than rats treated with only PTH. The lower bone strength thus appeared disproportionate to lower BMD, suggesting that anti-VEGF inhibits the ability of PTH to improve bone strength as much as the bone mass effect of PTH would suggest (Rhee et al., 2009). When adult male rats were given a bone anabolic dose of PTH or PTH combined with bevacizumab (BVZ) for 15d, PTH increased bone mass and bone formation, but those changes were blunted by BVZ (Prisby et al., 2011; Prisby et al., 2013). Rats given BVZ monotherapy had fewer blood vessels, with no significant differences from control rats in skeletal phenotype (Prisby et al., 2011; Prisby et al., 2013). Despite the importance of vascularity to both bone homeostasis and the anabolic action of PTH, the effects of low bone blood flow on bone strength and bone mass have not been studied. Importantly, anti-VEGF monotherapy does not appear to significantly influence bone formation and bone mass in adult rats.

Numerous pre-clinical studies of bone-active agents show concurrent, correlated effects on both bone strength and bone mass (PTH, GCs, N-BPs, etc.) (Mohan et al., 2017; Li et al., 1991; Isowa et al., 2010; Allen et al., 2006). Occasional pre-clinical studies have evaluated agents that affect bone strength with minor effects on BMD (Allen et al., 2006). Based on what has been learned about the maintenance of vascular integrity by clinical use of VEGF inhibitors (Senger, 2010; Murakami, 2012; Murakami and Simons, 2009; Maurea et al., 2016; Hu and Olsen, 2016a), our approach was to treat adolescent/young adult mice with anti-VEGF, an agent that reduces bone blood vessel number (Prisby et al., 2011) and then study bone blood flow, bone mass and bone strength. We hypothesized that bone blood flow is associated with bone strength independently of bone mass. While this type of agent inhibits the maintenance of vascular integrity (Murakami, 2012; Murakami and Simons, 2009; Maurea et al., 2016; Kamba and McDonald, 2007; Fish and Wythe, 2015; Baffert et al., 2006; Zeb et al., 2007) and causes low blood flow, its effects on bone mass and bone strength are currently unknown.

2. Materials and methods

2.1. Animals

Nine-week-old male BALB/cJ (n = 24) mice (Jackson Laboratory; Sacramento, CA. USA) were purchased and housed for seven days at the UC Davis Animal Facility. Mice were kept singly in plastic cages with a 12:12-hour dark:light cycle and a temperature range of 20–22 °C. They were fed commercial rodent chow (22/5 Rodent Diet; Teklad; Madison, WI) ad libitum. After one week, mice were body weight-randomized into either a rodent anti-VEGF monoclonal antibody group (anti-VEGF; B20-4.1.1; Genentech; South San Francisco, CA) (n = 12) (Tegnebratt et al., 2018; Jiang et al., 2014) or a vehicle group (VEH; n = 12; phosphate-buffered saline). Mice were then treated twice weekly for six weeks with anti-VEGF (5 mg/kg; 0.1 cc/100 g BW) or VEH by subcutaneous injection (Wu et al., 2012). Body weight was measured weekly. The study was carried out following recommendations in the Guide for the Care and Use of Laboratory Animals of the National Institutes of Health with the approval of the UC Davis Institutional Animal Care and Utilization Committee.

2.2. Bone blood flow measurement (in vivo ^{18}F-NaF-positron emission tomography/computed tomography (^{18}F-NaF-PET/CT) imaging)

Mice were anesthetized using isoflurane/O_2 (3% induction, 1.5–2% maintenance) for a total of 55 min. Anesthetized mice were secured on a portable scanning bed of a small-animal PET scanner (Inveon DPET, Siemens Healthcare; Knoxville, TN, USA) (Bao et al., 2009). The PET acquisition was initiated and ^{18}F-Na-fluoride (~9.25 MBq) was injected intravenously via a tail vein catheter. Dynamic imaging was performed and listmode data were collected for 45 min. After the PET scan was complete, the scanning bed with the mouse still secured was moved to an adjacent small-animal computed tomography (CT) scanner (Inveon, Siemens Healthcare; Knoxville, TN, USA), where a whole-body CT scan was performed. External fiducial markers on the scanning bed guided the subsequent registration of the PET and CT images.

The PET dynamic data were reconstructed into 43 time frames (12 × 10 s, 16 × 30 s, 10 × 60 s, 5 × 300 s) using the manufacturer's software. Analysis of ^{18}F-NaF uptake kinetics was carried out using the PMOD software (PMOD 3.802; PMOD Technologies Ltd.; Zurich, SW) of which the first 33 (15 min) were used. First, ellipsoidal volumes of interest (VOIs) for each distal femur were manually drawn on the PET image, based on the co-registered CT (Fig. 1). Next, compartmental modeling based on a 2-tissue, 4-parameter model (Hawkins et al., 1992) was employed to estimate specific rate constants for each VOI that described transport and binding of ^{18}F-NaF. The blood-input function
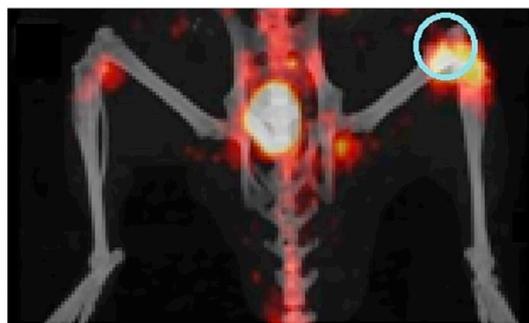

Fig. 1. Representative ^{18}F-NaF PET/CT maximum intensity projection image of lower half of mouse body during 0–15 min post ^{18}F-NaF injection. Femurs, tibias, lower spine, and feet are visible from CT scan (grayscale). Red-orange spots represent ^{18}F-NaF PET signal location. Note ellipsoidal VOI over distal femur. White area in center is bladder. (For interpretation of the references to colour in this figure legend, the reader is referred to the web version of this article.)

needed for compartmental modeling was derived from the images of the left ventricle of the heart. The primary rate constant derived for each VOI was K_1, the forward capillary transport parameter. K_1 (ml/cc/min) is the product of bone blood flow and the ^{18}F-NaF extraction fraction (Czernin et al., 2010). Because of the high single-passage extraction of ^{18}F-NaF (Wootton and Doré, 1986), K_1 correlates strongly with bone blood flow (Piert et al., 1998; Piert et al., 2001; Temmerman et al., 2008; Ottoy et al., 2017; Chen et al., 2015). In each mouse, K_1 was derived separately for each distal femur.

2.3. Necropsy

^{18}F-NaF PET/CT scanning was conducted the day before necropsy. At necropsy, mice were euthanized by CO_2 asphyxiation followed by cardiac puncture. Cervical dislocation was used as a secondary method of euthanasia. Both femurs were dissected free at the acetabulum and separated from the tibias. Lumbar vertebra 3–6 were dissected free from the other vertebrae. Both humeri were dissected free from the scapula and forelimb bones. All bones were cleansed gently of attached muscle, wrapped in saline-soaked gauze, and frozen at $-20\,°C$.

2.4. Biomechanical testing

2.4.1. Lumbar vertebral body 6 (compression)

The L6 vertebral body (LVB6), a trabecular bone rich site, was mechanically tested in axial compression. Specimens were thawed at room temperature for two hours. Posterior elements were trimmed from each LVB6 at the pedicle, and endplates were cut parallel using a low-speed, water-irrigated, circular bone saw (Isomet 1000; Buehler, Lake Forest, IL), such that the test specimens had a longitudinal axis length of ~1.5 mm. Specimens were rehydrated with phosphate-buffered saline prior to testing, and were kept hydrated during testing. Samples were affixed to loading platens with cyanoacrylate glue, then compressed to failure at 0.05 mm/s using an electromagnetic materials testing system (Bose ELF 3200; San Diego, CA USA). Customary variables relating to bone strength were calculated from the force vs. displacement curve (Makowski et al., 2014; Nyman et al., 2011a; Nyman et al., 2011b; Turner and Burr, 1993). These included ultimate load, yield load, stiffness, yield stress, and work to failure.

2.4.2. Femoral diaphysis (three-point bending)

Three-point bending tests of hydrated right femurs were performed using a servohydaulic material testing system (Instron DynaMight 8841; Norwood, MA) fitted with a linear variable displacement transducer (attached to the actuator) and a 100 N load cell (Honeywell; Columbus, OH; Model# 060-C863-02). Specimens were thawed at room temperature for two hours. The specimens were placed anterior surface down and medial side forward, and then loaded to failure at the midpoint, at 3 mm/min with a fixed lower span of 8 mm. One femur from the VEH group could not be stabilized during testing, leading to the exclusion of that bone's three point bending test data (see below). Customary whole-bone structural properties were determined from the force vs. displacement curve as above (Nyman et al., 2011a; Turner and Burr, 1993). Ultimate moment was calculated as (ultimate load X span/4).

2.5. Areal bone mass measurement (peripheral quantitative computed tomography (pQCT))

pQCT of the right humerus was performed to determine areal bone mass in trabecular and cortical bone regions. The humerus was scanned in 1 mm thick cross sections using a Stratec XCT Research M instrument (v5.40, Norland Medical Systems; Fort Atkinson, WI). The sites of interest were a 1 mm slice centered at 5 mm distal to the proximal end of the humerus (proximal metaphysis), and a 1 mm slice centered at the longitudinal midpoint of the humerus (mid-diaphysis or central region).

Bone mineral content (BMC, g), bone area (Ar, cm^2), and areal bone mineral density (BMD, mg/cm^2) were determined for trabecular bone of the proximal humeral metaphysis and cortical bone of the central femur (Brodt et al., 2003; Schmidt et al., 2003).

2.6. ^{1}H-nuclear magnetic resonance relaxometry (NMR)

Prior to the three-point bending test, volume fractions of bound water (BW), pore water (PW), and solid proton, were measured in the intact right femur using ^{1}H NMR relaxometry (Horch et al., 2011a). After thawing to room temperature, the femur was blotted to remove surface water and placed in a capped NMR-tube with 20 μL of deionized water in sealed glass (reference marker with a long $T_2 = ~2.5$ s). An in-house-built radio frequency (RF) coil with very low background proton signal (Horch et al., 2010) was used for excitation and signal reception. Upon placing the coil in a 4.7 T horizontal bore magnet (Varian Medical Systems, Santa Clara, CA), Carr-Purcell-Meiboom-Gill (CPMG) measurements with a total of 10,000 echoes were acquired at an echo spacing of 100 μs. The CPMG data vector was fitted to 256 decaying exponentials with time constants between 100 μs and 10 s and subject to non-negative and minimum curvature constraints to produce a T_2 spectrum (Fig. 3). The area of signal was integrated for three T_2 spectral components (0.172 ms to 0.65 ms for BW, 0.65 ms to 42 ms for PW, and 760 ms to 10 s for the reference marker). BW and PW areas were converted to volume using the ratio of the reference marker area to the known water volume, and then divided by the bone specimen volume measured by Archimedes' principle, to obtain BW and PW as a percentage.

2.7. Microcomputed tomography (MicroCT)

The right distal femoral metaphysis (DFM) and sixth lumbar vertebra (LV6) were imaged ex-vivo using a high-resolution scanner (VivaCT 40, Scanco Medical AG, Bassersdorf, Switzerland) at 70 kVp and 145 μA with scan settings that provided an isotropic voxel size of resolution of 10.5 μm in all three dimensions. Scanning of the DFM was initiated 1 mm proximal to the distal end of the bone and extended proximally for 250 slices. Scanning of LV6 was initiated at its caudal end and continued to its cranial end. 3D reconstruction of each scan was done with manufacturer's software. For the DFM, a secondary spongiosa VOI with a proximal boundary 0.2 mm proximal to the most proximal point of the growth cartilage-metaphyseal junction (GCMJ) and extending 150 slices proximal, was used. For LV6, the trabecular bone region of the body was analyzed. A VOI that started 0.1 mm cranial to the caudal GCMJ and ended 0.1 mm caudal to the cranial GCMJ was used. A trabecular-cortical boundary at 0.15 mm from the endocortical surface was established for each slice. All trabecular bone inside the boundary was evaluated. The methods for calculating bone volume (BV), total volume (TV), connectivity density, volumetric trabecular bone mineral density (vTb.BMD), trabecular tissue mineral density (Tb.TMD), trabecular thickness (Tb.Th), trabecular number (Tb.N), and structure model index (SMI) have been described (Bouxsein et al., 2010).

The right femoral diaphysis was imaged as above. Scanning was initiated 0.5 mm proximal to the mid-point of the bone and extended distally for 100 slices. From beam theory, the ultimate moment is directly proportional to the cross-sectional geometry factor, section modulus (I_{min}/c_{min}), where I_{min} is the moment of inertia for bending within the anterior-posterior plane and c_{min} is the distance between neutral axis (zero stress) and outer most bone surface in the direction of loading. I_{min}/c_{min} was calculated using Slice 51 of the scan.

2.8. Statistical analysis

The group means and standard deviations were calculated for all variables (GraphPad Prism 7.00 {GraphPad Software, La Jolla, CA
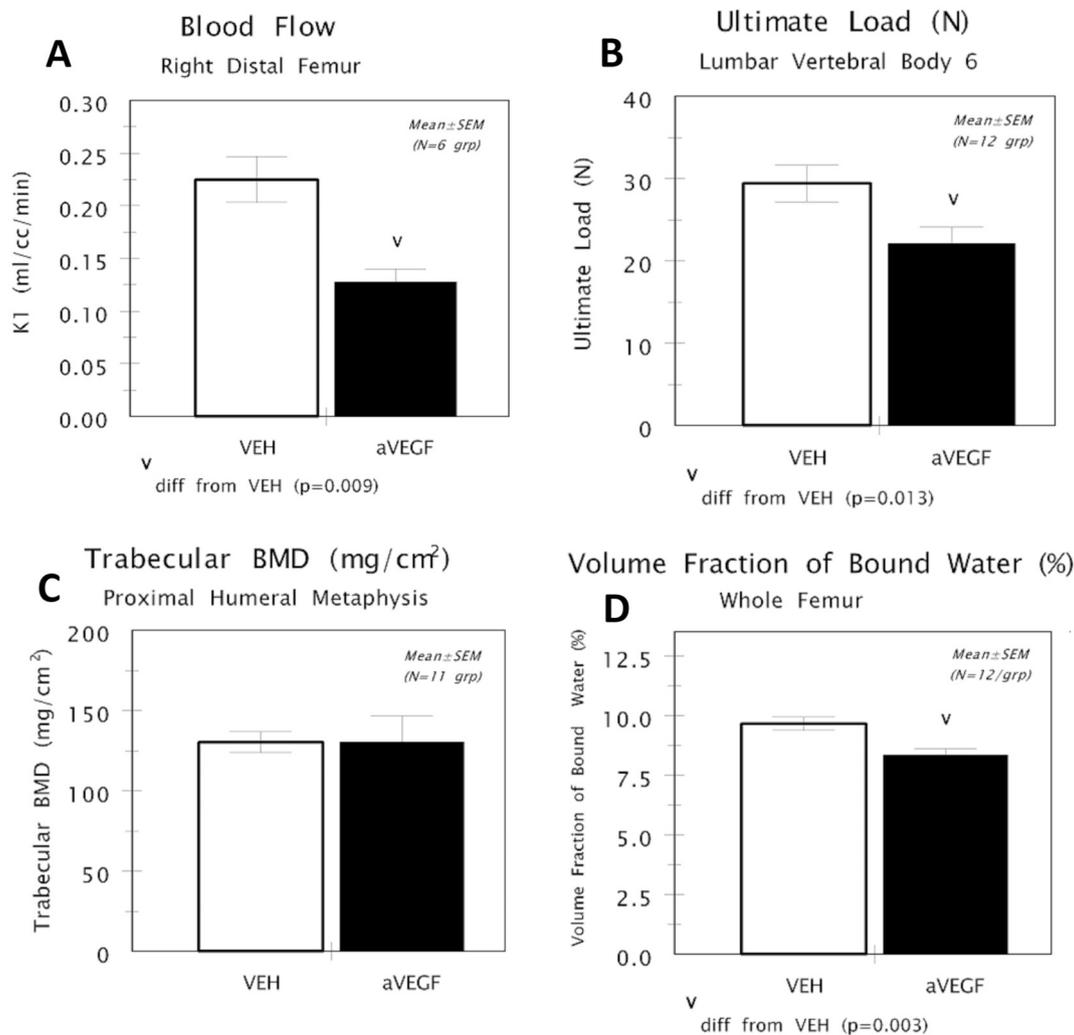
Fig. 2. Assessment of bone blood flow, bone strength, bone mass, and bone water.
The common tissue measured in 2A-2C is red marrow trabecular bone regions.
A- Blood Flow in Right Distal Femur. Blood flow was 43% lower in anti-VEGF-treated mice than in VEH-treated mice. B- Ultimate Load of Lumbar Vertebral Body 6- Ultimate load was 25% lower in anti-VEGF-treated than in VEH-treated mice. C- Trabecular Bone Mineral Density (BMD) in Right Proximal Humeral Metaphysis- Trabecular BMD was the same in anti-VEGF-treated and VEH-treated mice. D- Bound Water Volume Fraction in the Femur- Bound water volume fraction in the whole femur was 14% lower in anti-VEGF-treated mice than in VEH-treated mice. (For interpretation of the references to color in this figure legend, the reader is referred to the web version of this article.)

USA}]. The Mann-Whitney U test was used to assess intergroup differences. Differences were considered significant at $p < 0.05$.

Pearson's correlation coefficient for end of study body weight to bound water and pore water was calculated separately for the VEH and anti-VEGF groups.

To determine whether the structural-dependent bending strength (ultimate moment) of the central femur was solely explained by the cross-sectional geometry (section modulus) or helped by other properties of the femur (that differed between treatment groups), linear regressions were performed using general linear models [Stata 11.0, (StataCorp; College Station, TX USA)] in which the interaction term was excluded if not significant ($p > 0.05$).

3. Results

3.1. Pre-necropsy body weight and bone blood flow (Table 1, Fig. 2A)

Final body weight was 10% lower ($p = 0.001$) in anti-VEGF-treated mice than in VEH-treated mice. Distal femoral blood flow, as measured by K_1, at both the right and left sides was 43% lower ($p = 0.009$) in anti-VEGF-treated than in VEH-treated mice (Fig. 2A).
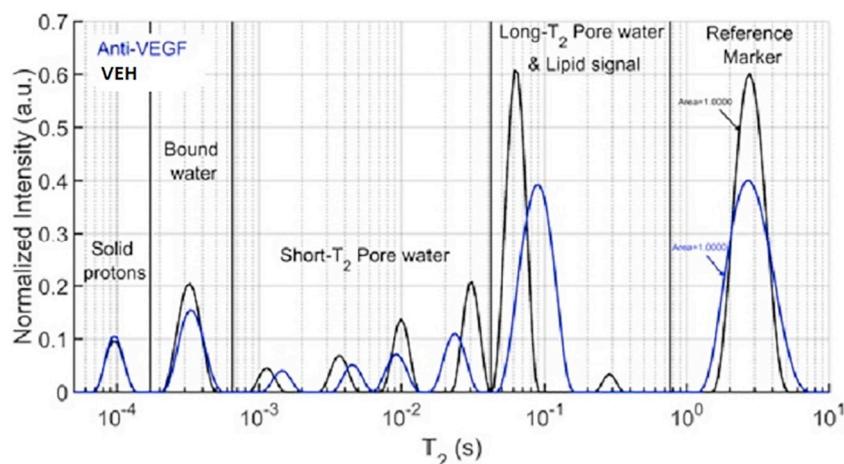
3.2. Trabecular and cortical bone strength (Table 2, Fig. 2B)

Ultimate load of LVB6 was 25% lower (Fig. 2B, $p = 0.013$) and stiffness was 44% lower (Table 2, $p = 0.044$) in anti-VEGF-treated mice than in VEH-treated mice. Work to failure at LVB6 was not affected by anti-VEGF. Though ultimate load at the central femur was 8% lower ($p = 0.032$) in anti-VEGF-treated than in VEH-treated mice, all other biomechanical properties at the central femur were the same in the two groups (Table 2).

3.3. Bone mass of humerus (Table 1, Fig. 2C)

Metaphyseal trabecular BMC, BMD (Fig. 2C), and bone area were the same in anti-VEGF-treated and VEH-treated mice. Cortical BMD was 1.9% higher ($p = 0.045$) and cortical thickness was 6.1% higher ($p = 0.024$) in anti-VEGF-treated mice than in VEH-treated mice (Table 1). Cortical BMC and cortical area also trended higher in anti-VEGF-treated mice than in VEH-treated mice (Table 1).

Fig. 3. Assessment of bone water ([1]H-nuclear magnetic resonance relaxometry (NMR)).

Representative relaxation time constant (T_2) spectra from femurs of anti-VEGF (blue) and VEH (black) mice. Normalized intensity (y-axis) vs. log Relaxation Time (sec) (x-axis)

The solid protons involved in covalent bonds (Solid Proton Band with peak near $T_2 = 10^{-4}$ s) relax faster than the water protons participating in hydrogen bonding within the organic matrix (Bound Water Band with peak near $T_2 = 4 \times 10^{-4}$ s). The water protons participating in hydrogen bonding with this organic matrix in turn relax faster than the water protons residing in pores (Short T_2 Pore Water bands ranging between $T_2 = 10^{-3}$ s and $T_2 = 4 \times 10^{-4}$ s). The reference marker is a known volume of water. The Reference Marker thus has the slowest relaxation (i.e., longest T_2 values between 1 and 10s). Because marrow was present, the area under the pore water signals was integrated between the two vertical lines spanning 6.5×10^{-4} s $\ll T_2 < \sim 4 \times 10^{-2}$ s). Therefore, this measurement not only excluded water in large pores, but also avoided the lipid signal. Both the area of the Bound Water Band and the area of the Pore Water Band were converted to the volume of water using the area under the Reference Marker band.

Note that all peaks for the representative T_2 spectrum from the anti-VEGF mouse are lower than those for the VEH mouse. (For interpretation of the references to color in this figure legend, the reader is referred to the web version of this article.)

3.4. Bone water endpoints (Table 2, Fig. 2D)

Volume fraction of bound water of the left femur was 14% lower (Fig. 2D, p = 0.003) in anti-VEGF-treated than in VEH-treated mice. No other NMR properties were affected by anti-VEGF (Table 2). There was no significant correlation of volume fraction of bound water or pore water to ending body weight (Table 4).

3.5. Microarchitecture (Table 3)

Connectivity density in the lumbar vertebral body was 11% higher (p = 0.028) and trabecular thickness was 7% lower (p = 0.028) in anti-VEGF-treated mice than in VEH-treated mice (Table 3). No other microarchitectural endpoints in the lumbar vertebral body were affected by anti-VEGF.

At the distal femoral metaphysis, SMI was 11% higher (p = 0.024) and trabecular thickness was 21% higher (p = 0.002) in anti-VEGF-treated than VEH-treated mice (Table 3). However, no other microarchitectural endpoints were affected by anti-VEGF. Tissue mineral density of trabecular bone (Tb.TMD) was 7% higher (p = 0.001) in anti-VEGF-treated than in VEH-treated mice (Table 3).

No structural endpoints at the central femur were significantly affected by anti-VEGF. Tissue mineral density of cortical bone (Ct.TMD)

Table 2
Trabecular and cortical bone strength and ^{1}H NMR endpoints.

Endpoint		Vehicle		anti-VEGF		
	Units	N	Mean ± SD	N	Mean ± SD	p =
Lumbar vertebral body 6 (compression) (trabecular)						
Stiffness	N/mm	12	168.6 ± 97.3	11	105.0 ± 53.7	0.044
Work to failure	J	12	8.69 ± 4.75	11	6.66 ± 3.19	0.413
Right central femur (3 point bending) (cortical)						
Ultimate load	N	11	24.58 ± 1.72	12	22.69 ± 2.03	0.032
Yield load	N	11	19.49 ± 1.70	12	18.48 ± 2.10	0.316
Stiffness	N/mm	11	142.8 ± 12.7	12	137.4 ± 13.4	0.316
Yield stress	N/mm²	11	178.2 ± 20.9	12	179.2 ± 17.0	0.880
Work to failure	N-mm	11	5.56 ± 0.82	12	5.80 ± 1.06	0.651
^{1}H NMR endpoints						
Solid proton	%	12	3.92 ± 0.42	12	3.86 ± 0.51	0.799
Pore water volume fraction	%	12	15.49 ± 1.19	12	16.81 ± 3.44	0.160

p = Mann-Whitney U.

was 1.4% lower (p = 0.011) and volumetric bone mineral density (Ct.BMD) was 1.5% lower (p = 0.007) in anti-VEGF-treated than in VEH-treated mice (Table 3).

Table 1
Body weight, bone blood flow, and bone mass of humerus (pQCT).

Endpoint		Vehicle		Anti-VEGF		
	Units	N	Mean ± SD	N	Mean ± SD	p =
Final body weight	g	12	29.6 ± 1.3	12	26.6 ± 2.2	0.001
Blood flow						
Left distal femur	ml/cc/min	6	0.216 ± 0.063	6	0.122 ± 0.034	0.009
Humerus bone mass						
Proximal metaphysis						
Trabecular BMC	mg	10	57 ± 9	11	59 ± 24	0.919
Trabecular area	cm²	12	0.429 ± 0.054	12	0.443 ± 0.025	0.887
Diaphysis						
Cortical BMC	mg	12	1006 ± 108	12	1091 ± 85	0.078
Cortical BMD	mg/cm²	12	1199 ± 23	12	1222 ± 33	0.045
Cortical area	cm²	12	0.839 ± 0.079	12	0.892 ± 0.053	0.101
Cortical thickness	mm	12	0.392 ± 0.022	12	0.416 ± 0.022	0.024

BMC- bone mineral content.
BMD- bone mineral density.
p = Mann-Whitney U.

Table 3
Microarchitecture of vertebral body and left femur.

Endpoint	Units	Vehicle		anti-VEGF		p =
		N	Mean ± SD	N	Mean ± SD	
Lumbar vertebral body 6						
BV/TV	%	9	26.8 ± 2.2	11	25.0 ± 2.7	0.074
Connectivity density	mm^{-2}	9	230.2 ± 33.0	11	260.6 ± 25.2	0.028
SMI	–	9	0.370 ± 0.255	11	0.496 ± 0.269	0.277
Trabecular number	mm^{-1}	9	4.96 ± 0.16	11	4.96 ± 0.38	0.590
Trabecular thickness	mm	9	0.053 ± 0.003	11	0.049 ± 0.003	0.028
Volumetric Tb.BMD	$mgHA/cm^3$	12	209.4 ± 26.9	12	189.8 ± 31.2	0.117
Tb.TMD	$mgHA/cm^3$	12	722 ± 17	12	722 ± 20	0.977
Left distal femur						
BV/TV	%	12	15.7 ± 3.2	12	16.9 ± 2.8	0.242
Connectivity density	mm^{-2}	12	188.7 ± 72.5	12	133.4 ± 32.1	0.060
SMI	–	12	2.02 ± 0.34	12	2.23 ± 0.22	0.024
Trabecular number	mm^{-1}	12	4.92 ± 0.69	12	4.77 ± 0.32	0.378
Trabecular thickness	μm	12	46.9 ± 4.1	12	56.9 ± 9.0	0.002
Volumetric Tb.BMD	$mgHA/cm^3$	12	160.5 ± 27.9	12	175.2 ± 20.3	0.127
Tb.TMD	$mgHA/cm^3$	12	724 ± 15	12	774 ± 21	0.001
Left central femur						
Cortical area	mm^2	11	1.031 ± 0.062	12	0.988 ± 0.053	0.169
Total area	mm^2	11	1.751 ± 0.120	12	1.712 ± 0.109	0.525
Moment of inertia	mm^4	11	0.135 ± 0.017	12	0.123 ± 0.015	0.089
Cortical area/total area	%	11	58.9 ± 1.8	12	57.8 ± 1.2	0.136
Cortical thickness	mm	11	0.250 ± 0.013	12	0.247 ± 0.006	0.695
Volumetric Ct.BMD	$mgHA/cm^3$	11	1065 ± 11	12	1053 ± 21	0.032
Ct.TMD	$mgHA/cm^3$	12	1091 ± 12	12	1078 ± 11	0.037

p = Mann-Whitney U.
TMD- tissue mineral density.
HA-hydroxyapatite.

3.6. Multivariate explanation of strength

From beam theory, the ultimate moment applied to a femur is directly proportional to the section modulus of the mid-shaft (i.e., I_{min}/c_{min}). Section modulus explained 63.9% of the variance in ultimate moment (Fig. 4). Standardized coefficients (β) for explanatory variables indicated that BW (p = 0.007) helped section modulus explain the variance in ultimate moment, whereas Ct.TMD of the diaphysis was not useful (Table 5).

4. Discussion

Using an anti-VEGF antibody to inhibit blood flow, the present study may have established an association between bone blood flow
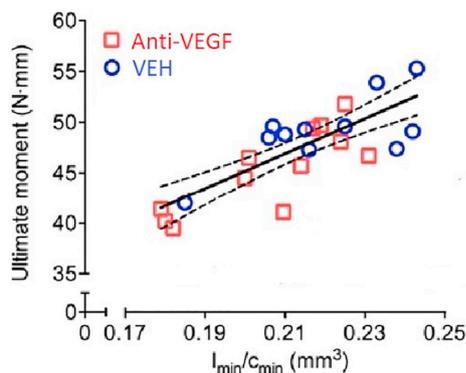

Fig. 4. Ultimate moment vs. I_{min}/c_{min}.
From beam theory, ultimate moment is directly proportional to the cross-sectional geometry factor I_{min}/c_{min}, where I_{min} is the moment of inertia for bending within the anterior-posterior plane and c_{min} is the distance between neutral axis (zero stress) and outermost bone surface in the direction of loading. If anti-VEGF affected the material strength of the bone matrix, then either the slope or y-intercept would differ between the groups, which they did not (P > 0.10).

and trabecular bone quality. Both blood flow, assessed by in vivo ^{18}F-NaF-PET/CT of the distal femur, and bone strength, assessed by an ex vivo compression test of LVB6, were lower in anti-VEGF-treated mice than in VEH-treated mice that showed no treatment-related differences in bone mass. Specifically, BMD and BMC of the proximal humeral metaphyseal trabecular region, as well as bone volume fraction and volumetric BMD of the distal femoral metaphysis and LVB6, were not affected by anti-VEGF, while ultimate load, the principle indicator of whole bone strength, was 25% lower in LVB6 of anti-VEGF-treated mice than in VEH-treated mice. Therefore, low bone blood flow appears to cause low bone strength without causing low bone mass, indicating that it may reduce bone strength through an effect on bone quality. These data support our hypothesis that bone blood flow is associated with bone strength independently of bone mass.

Our results parallel data from F344 rats, in which an age-related decrease in bone blood flow was associated with lower ultimate bending stress of the central femur despite higher femoral BMD (Bloomfield et al., 2002). An experiment that applies a second class of anti-angiogenic agents, such as tyrosine kinase inhibitors (Lopez et al., 2019; Bai and Zhang, 2018), would be necessary to reveal whether low bone blood flow itself, rather than an intrinsic effect of this anti-VEGF antibody, causes low bone strength. In any case, our data indicate that bone blood flow is positively associated with whole bone strength with no effect on bone mass in red marrow trabecular bone rich regions (distal femoral metaphysis, LVB6, and proximal humeral metaphysis), suggesting that bone blood flow is a bone property that influences bone quality.

VEGF supports vascular integrity in all organs by both maintaining the vasculature and stimulating angiogenesis (Senger, 2010; Murakami, 2012; Murakami and Simons, 2009; Maurea et al., 2016; Hu and Olsen, 2016a). We chose anti-VEGF with the aim of improving the understanding of sources of excessive bone fragility in GC-induced osteoporotic (GIOP) patients. Unlike GCs that reduce both BMD and bone blood flow (Weinstein et al., 2010; Mohan et al., 2017), we envisioned anti-VEGF as a bone mass-neutral agent that would act as a biological tool that specifically reduces bone blood flow, allowing direct studies of

Table 4
Pearson correlation coefficients of ending body weight to bone water variables.

Variable	Group	R =	p =	N
Volume fraction of bound water	VEH	0.3966	0.2018	12
Volume fraction of pore water	VEH	0.1195	0.7114	12
Volume fraction of bound water	Anti-VEGF	0.2341	0.4640	12
Volume fraction of pore water	Anti-VEGF	0.0127	0.9688	12

the effect of low blood flow on bone strength, without the uncertainty introduced by the negative BMD effects of GCs that themselves decrease bone strength.

Identifying a physical property of bone tissue that is positively-related to both bone blood flow and bone strength could improve the current understanding of how bone blood flow affects bone strength. Therefore, we measured volume fraction of bound water (BW), the amount of water interacting with the bone matrix, in the whole femur, a property known to be related to bone strength (Nyman et al., 2006). While anti-VEGF had no significant effect on bone mass and microarchitectural properties of trabecular bone regions of the humerus and femur, whole femur BW in anti-VEGF mice was lower than in VEH-treated mice. Importantly, there was no correlation of BW endpoints to end of study body weight in either treatment group (Table 4). Both low bone blood flow and volume fraction of BW are thus associated with low bone strength. Volume fraction of BW also significantly helped the bone geometry factor related to bending explain ultimate moment in cortical bone (Table 5). This suggests that clinical assessment of BW by MRI (Manhard et al., 2017) could lead to a better understanding of the bone strength/bone mass discrepancy observed in patients treated with GCs, patients with diabetes, patients with peripheral vascular disease, and patients with osteopenia who experience fragility fracture.

Three-point bending tests of machined specimens of human cortical bone show that BW is positively correlated with ultimate stress (Horch et al., 2011b) and crack initiation toughness (Granke et al., 2015). While the important determinants of BW have yet to be identified, the present study suggests that bone blood flow could affect those determinants, that include factors that affect the number of hydrogen bonds between hydrophilic compounds within the organic matrix and water, and the electrostatic attractions between ions on the surfaces of mineral crystals and water (i.e. water molecules have a dipole moment). Such bonds imbue stretchability to the Type I collagen of bone and possibly mediate the transfer of stress between the flexible collagen and the rigid mineral phase, thereby increasing fracture resistance (Timmins and Wall, 1977). For mice, in which cortical bone does not undergo ambient osteonal remodeling, BW is inversely proportional to tissue mineral density (TMD) (Mody et al., 2018). Evaluation of the effect of anti-VEGF on those determinants in future studies could add additional clarity.

A direct relationship of bone blood flow to bone strength may be clinically relevant to specific patient groups. Considering only areal BMD, GC-treated (Van Staa et al., 2003; Balasubramanian et al., 2018; Saag et al., 2009; Weinstein et al., 2010), diabetic (Sellmeyer et al.,

2016; Rubin, 2017), and hyperhomocysteinemic patients (Behera et al., 2017; Blouin et al., 2009) have unusually high fracture risk. Though understudied bone properties, such as bone blood flow, may explain the excessive fracture risk, investigating those properties requires innovative approaches. For instance, GCs are dual action agents (Weinstein et al., 2010; Mohan et al., 2017) that cause not only low bone blood flow and vascularity, but also low BMD and trabecular thinning (Van Staa et al., 2003; Balasubramanian et al., 2018; Briot, 2018; Dempster et al., 1983). The latter conditions cause increased fracture risk. Thus, the exact cause of low bone strength (or increased fracture risk) cannot be determined experimentally using dual action agents like GCs as a research tool, because the two actions, bone blood flow reduction and loss of BMD, cannot be easily dissociated. In our experiment, anti-VEGF served as a single action therapeutic that reduced bone strength with no effect on bone mass, enabling a focus on the relationship of bone blood flow to bone strength. Diabetic patients have well-documented problems with low blood flow (Beckman and Creager, 2016; King and Grant, 2016). Patients with hyperhomocysteinemia display both low bone blood flow and abnormal bone matrix quality (Behera et al., 2017; Fratoni and Brandi, 2015; Tyagi et al., 2011a; Tyagi et al., 2011b). While directly-measured bone blood flow data in GC and diabetic patients are limited, both groups have increased risk of coronary artery and peripheral vascular disease. If those vascular problems also manifest in bone as low blood flow, our study could reflect the condition of these patients, suggesting that low bone blood flow explains a portion of their excess bone fragility. Half of all fragility fractures occur in individuals with osteopenia (BMD T-score < −1.0, but > −2.5), rather than osteoporosis (T-score < −2.5) (Kanis et al., 1994; Fonseca et al., 2014). As with GC and diabetic patients, studies of bone blood flow in BMD-matched osteopenic patients who have (or have not) experienced fragility fractures, could be used to examine the relationship of bone blood flow to excessive bone fragility (Rizzo et al., 2018; Polly et al., 2012).

Anti-VEGF (e.g., bevacizumab) is an FDA-approved adjuvant cancer treatment that reduces tumor angiogenesis and increases progression-free survival in colorectal, ovarian, and cervical cancer; and clear cell renal and non small cell lung carcinoma patients. Its documented adverse effects include hypertension, bleeding, abnormal blood clotting, myocardial infarction, cerebral vascular accident, inhibition of wound healing, and intestinal perforation (Fucà et al., 2018; Raouf et al., 2018; Chen et al., 2006; Lee et al., 2018). All potentially indicate mechanism-based, negative effects on vasculature of the non-cancerous portions of the body (Kamba and McDonald, 2007; Fish and Wythe, 2015; Baffert et al., 2006; Zeb et al., 2007). Our data suggest that it is reasonable to think that low bone blood flow may cause increased fracture risk not only in GC-treated subjects or in patients with diabetes, peripheral vascular disease, or osteopenia, but also in patients treated with anti-angiogenic agents. All these diseases and medications would likely express their negative effects on bone strength in humans as increased fracture risk not mediated through BMD, making trials that measure BMD without monitoring fracture uninformative.

These data may also provide additional information about how the

Table 5
General linear models for ultimate moment.

I_{min}/c_{min}	Covariate	Coefficient	Interaction	Adj-R^2 (%)
$\beta = 0.799$ (p < 0.0001)	–	–	–	62.2
(p = 0.671)	Ct.Th	(p = 0.690)	(p = 0.781)	65.7
$\beta = 0.730$ (p < 0.0001)	Ct.Th	$\beta = 0.261$ (p = 0.052)	NI	67.3
(p = 0.425)	Ct.TMD	(p = 0.414)	(p = 0.464)	63.8
$\beta = 0.779$ (p < 0.0001)	Ct.TMD	(p = 0.137)	NI	64.6
(p = 0.991)	BW	(p = 0.634)	(p = 0.495)	72.1
$\beta = 0.746$ (p < 0.0001)	BW	$\beta = 0.341$ (p = 0.007)	NI	72.8

BW- volume fraction of bound water.
NI = no interaction.

actions of existing pharmaceutical treatments for osteoporosis reduce fracture risk. Teriparatide (PTH) is a bone anabolic agent that reduces fracture risk much more than its effects on areal BMD would indicate (Chen et al., 2006). Our data suggest that part of that discrepancy might be explained by a positive effect of PTH on bone blood flow. Though some data indicate that PTH enhances blood flow through VEGF-dependent mechanisms, the findings are not universal. PTH restores endothelium dependent vasodilation in adult rats to the level in young rats (Lee et al., 2018) through activation of nitric oxide and protein kinases A and C (PKA and PKC) signaling (Benson et al., 2016). PTH-related vasodilatation of bone arteries appears dependent upon VEGF signaling within the vascular endothelium (Prisby et al., 2013; Isowa et al., 2010). PTH increases the release of VEGF from osteoblasts and osteocytes to stimulate new blood vessel formation (Isowa et al., 2010). PTH knockout mice display delayed fracture healing associated with reduced VEGF production from bone marrow stem cell derived osteoblasts (Ding et al., 2018). On the other hand, though PTH improves the vasodilatory capacity of blood vessels, it decreases blood vessel number in trabecular bone regions (Prisby et al., 2011). Though controversy exists concerning the effects of PTH on bone vasculature, our data might point to trials that study bone blood flow in teriparatide patients, to determine if positive bone blood flow effects of teriparatide explain a portion of its anti-fracture efficacy.

Some shortcomings of this experiment should be noted. Though we evaluated bone blood flow in a trabecular rich bone region using ^{18}F-NaF PET/CT, we were unable to evaluate bone blood flow in a cortical bone region, because of the intrinsic spatial resolution limitations of PET and/or the low vascularity of cortical bone. Efforts are underway to overcome this problem using partial volume correction methods (Soret et al., 2007) and terminal ^{18}F-NaF PET/CT scans that permit higher radiation doses that could better visualize regions with low blood flow. We measured bone blood flow, bone mass, and bone strength in three different trabecular bone rich sites (distal femur or distal femoral metaphysis, lumbar vertebral body, and proximal humeral metaphysis, respectively). The distal femur and proximal humerus are from the appendicular skeleton, while the lumbar vertebral body is from the axial skeleton. The three sites were chosen in spite of their location in different skeletal regions, because they are red marrow trabecular bone sites that display similar responses to currently prescribed bone-active agents. One should recognize that their individual responses to anti-VEGF may differ and were not evaluated here by traditional histo-morphometric methods. We were unable to measure bone blood flow in an anatomical site that expresses increased bone fragility in osteoporotic subjects (i.e., LVB6), because the ^{18}F-NaF PET signal in LVB6 cannot be separated from signal in overlying soft tissue or surrounding cortical portions of the whole vertebra. We were unable to measure bone water in trabecular bone regions. In future experiments, it should be possible to use pQCT to measure BMC and BMD in LVB6 before mechanical testing, distal femur BMC and BMD after ^{18}F-NaF PET/CT, and central femur BMC and BMD where ^{18}F-NaF PET/CT may eventually be possible. Administration of anti-VEGF began when mice were age 10 weeks, a time when bone elongation is slowing and the skeleton is best considered adolescent. Future studies that aim to interrogate the mature skeleton should start treatment in mice aged 18–20 weeks, an age at which the skeleton is considered mature adult.

5. Conclusions

Six weeks treatment of young adult mice with anti-VEGF appears to have caused low bone blood flow, bone strength, and bound water with no effect on bone mass. These data may suggest that bone blood flow is a novel bone property that affects bone quality.

Author statement

The following individual contributed, respectively to: study design/

planning (DBK, NEL), experimental conduct (WY, XPL, KS); data collection (JSN, SU, AJC, KS, XPL, JIA, WY); data analysis (JSN, DBK, AJC), original draft (DBK, NEL); revised draft (NEL, JSN, AJC, JIA, DBK).

Declaration of Competing Interest

Authors declare that they have no conflicts of interest in connection with this study.

Transparency document

The Transparency document associated with this article can be found, in online version.

References

Allen, M.R., Iwata, K., Sato, M., Burr, D.B., 2006. Raloxifene enhances vertebral mechanical properties independent of bone density. Bone 39, 1130–1135. https://doi.org/10.1016/j.bone.2006.05.007.

Baffert, F., Le, T., Sennino, B., et al., 2006. Cellular changes in normal blood capillaries undergoing regression after inhibition of VEGF signaling. Am Jour Physiology 290, H547–H559.

Bai, Z.G., Zhang, Z.T., 2018. A systematic review and meta-analysis on the effect of angiogenesis blockade for the treatment of gastric cancer. Onco Targets Ther 11, 7077–7087. https://doi.org/10.2147/OTT.S169484. (eCollection 2018).

Balasubramanian, A., Wade, S.W., Adler, R.A., Saag, K., Pannacciulli, N., Curtis, J.R., 2018. Glucocorticoid exposure and fracture risk in a cohort of US patients with selected conditions. J. Bone Miner. Res. 33 (10), 1881–1888. https://doi.org/10.1002/jbmr.3523.

Bao, Q., Newport, D., Chen, M., Stout, D.B., Chatziioannou, A.F., 2009. Performance evaluation of the Inveon dedicated PET preclinical tomograph based on the NEMA-NU4 standards. Jour Nucl Med 50 (3), 401–408. https://doi.org/10.2967/jnumed.108.056374.

Beckman, J.A., Creager, M.A., 2016. Vascular complications of diabetes. Circ. Res. 118 (11), 1771–1785. https://doi.org/10.1161/CIRCRESAHA.115.306884.

Behera, J., Bala, J., Nuru, M., Tyagi, S.C., Tyagi, N., 2017. Homocysteine as a pathological biomarker for bone disease. J. Cell. Physiol. 232 (10), 2704–2709. https://doi.org/10.1002/jcp.25693.

Benson, T., Menezes, T., Campbell, J., Bice, A., Hood, B., Prisby, R., 2016. Mechanisms of vasodilation to PTH (1-84), PTH (1-34), and PTHrP (1-34) in rat bone resistance arteries. Osteoporos. Int. 27 (5), 1817–1826.

Bloomfield, S.A., Hogan, H.A., Delp, M.D., 2002. Decreases in bone blood flow and bone material properties in aging Fischer-344 rats. Clin Orthop Rel Res 396, 248–257.

Blouin, S., Thaler, H.W., Korninger, C., Schmid, R., et al., 2009. Bone matrix quality and plasma homocysteine levels. Bone 44 (5), 959–964. https://doi.org/10.1016/j.bone.2008.12.023.

Bouxsein, M.L., Boyd, S.K., Christiansen, B.A., Guldberg, R.E., Jepsen, K.J., Muller, R., 2010. Guidelines for assessment of bone microstructure in rodents using MicroCT. J Bone Min Res 25, 1468–1486.

Briot, K., 2018. Bone and glucocorticoids. Ann Endocrinol (Paris) 79 (3), 115–118. https://doi.org/10.1016/j.ando.2018.04.016.

Brodt, M.D., Pelz, G.B., Taniguchi, J., Silva, M.J., 2003. Accuracy of peripheral quantitative computed tomography (pQCT) for assessing area and density of mouse cortical bone. Calcif. Tissue Int. 73 (4), 411–418.

Chang, A., Easson, G.W., Tang, S.Y., 2018. Clinical measurements of bone tissue mechanical behavior using reference point indentation. Clinic Rev Bone Miner Metab 16, 87–94. https://doi.org/10.1007/s12018-018-9249-9.

Chen, P., Miller, P.D., Delmas, P.D., Misurski, D.A., Krege, J.H., 2006. Change in lumbar spine BMD and vertebral fracture risk reduction in teriparatide-treated post-menopausal women with osteoporosis. J. Bone Miner. Res. 21 (11), 1785–1790 Nov.

Chen, Y.J., Rosario, B.L., Mowrey, W., Laymon, C.M., Lu, X., Lopez, O.L., et al., 2015. Relative 11C-PiB delivery as a proxy of relative CBF: quantitative evaluation using single-session 15O-water and 11C-PiB PET. J. Nucl. Med. 56, 1199 ± 205. https://doi.org/10.2967/jnumed.114.152405 PMID: 26045309.

Cummings, S.R., Black, D.M., Thompson, D.E., et al., 1998. Effect of alendronate on risk of fracture in women with low bone density but without vertebral fractures: results from the fracture intervention trial. JAMA 280, 2077–2082.

Cummings, S.R., Karpf, D.B., Harris, F., Genant, H.K., Ensrud, K., et al., 2002. Improvement in spine BMD and reduction in risk of vertebral fractures during treatment with antiresorptive drugs. Am. J. Med. 112, 281–289.

Czernin J, Satyamurthy N, Schiepers C. Molecular mechanisms of bone ^{18}F-NaF deposition, J. Nucl. Med.. 2010; 51(12):1826–9.

Delmas, P.D., Seeman, E., 2004. Changes in BMD explain little of the reduction in vertebral or nonvertebral fracture risk with anti-resorptive therapy. Bone 34, 599–604.

Dempster, D.W., Arlot, M.A., Meunier, P.J., 1983. Mean wall thickness and formation periods of trabecular bone packets in GIOP. Calcif. Tissue Int. 35, 410–417.

Ding, Q., Sun, P., Zhou, H., Wan, B., Yin, J., Huang, Y., Li, Q., Yin, G., Fan, J., 2018. Lack of endogenous PTH delays fracture healing by inhibiting VEGF-mediated angiogenesis. Int. J. Mol. Med. 42 (1), 171–181.

Fish, J.E., Wythe, J.D., 2015. The molecular regulation of arteriovenous specification and maintenance. Dev. Dyn. 244 (3), 391–409. https://doi.org/10.1002/dvdy.24252.

Fonseca, H., Moreira-Goncalves, D., Coriolano, H.J., Duarte, J.A., 2014. Bone quality: the determinants of bone strength and fragility. Sports Med. 44 (1), 37–53. https://doi.org/10.1007/s40279-013-0100-7. Jan.

Fratoni, V., Brandi, M.L., 2015. B vitamins, homocysteine and bone health. Nutrients 7 (4), 2176–2192. https://doi.org/10.3390/nu7042176.

Fucà, G., deBraud, F., DiNicola, M., 2018. Immunotherapy-based combinations: an update. Curr. Opin. Oncol. 30 (5), 345–351. https://doi.org/10.1097/CCO.0000000000000466.

Garnero, P., 2012. The contribution of collagen crosslinks to bone strength. Bonekey Rep 1, 182. https://doi.org/10.1038/bonekey.2012.182.

Granke, M., Makowski, A.J., Uppuganti, S., Does, M.D., Nyman, J.S., 2015. Identifying novel clinical surrogates to assess human bone fracture toughness. J. Bone Miner. Res. 30, 1290–1300. https://doi.org/10.1002/jbmr.2452.

Harris, S.T., Watts, N.B., Genant, H.K., McKeever, C.D., Hangartner, T., et al., 1999. Effects of risedronate treatment on vertebral and nonvertebral fractures in women with postmenopausal osteoporosis: a randomized controlled trial. Vertebral Efficacy with Risedronate Therapy (VERT) Study Group. JAMA 282, 1344–1352.

Hawkins, R.A., Choi, Y., Huang, S.C., Hoh, C.K., Dahlbom, M., et al., 1992. Evaluation of the skeletal kinetics of fluorine-18-fluoride ion with PET. J. Nucl. Med. 33, 633–642.

Hirche, C., Xiong, L., et al., 2017. Vascularized versus non-vascularized bone grafts in the treatment of scaphoid non-union. J Orthop Surg (Hong Kong) 25 (1), 2309499016684291.

Horch, R.A., Wilkens, K., Gochberg, D.F., Does, M.D., 2010. RF coil considerations for short-T2 MRI. Magn. Reson. Med. 64 (6), 1652–1657 Dec.

Horch, R.A., Gochberg, D.F., Nyman, J.S., Does, M.D., 2011a. Non-invasive predictors of human cortical bone mechanical properties: T2-Discriminated 1H NMR compared with high resolution X-ray. PLoS One 6 (1), e16359 Jan 21.

Horch, R.A., Gochberg, D.F., Nyman, J.S., Does, M.D., 2011b. Non-invasive predictors of human cortical bone mechanical properties: T(2)-discriminated H NMR compared with high resolution X-ray. PLoS One 6 (1), e16359. https://doi.org/10.1371/journal.pone.0016359. Jan 21.

Hu, K., Olsen, B.R., 2016a. The roles of VEGF in bone repair and regeneration. Bone 91, 30–38. https://doi.org/10.1016/j.bone.2016.06.013.

Hu, K., Olsen, B.R., 2016b. Osteoblast-derived VEGF regulates osteoblast differentiation and bone formation during bone repair. J. Clin. Invest. 126 (2), 509–526. https://doi.org/10.1172/JCI82585.

Isowa, S., Shimo, T., Ibaragi, S., Kurio, N., et al., 2010. PTHrP regulates angiogenesis and bone resorption via VEGF expression. Anticancer Res. 30 (7), 2755–2767.

Jiang, X., Engelbach, J.A., Yuan, L., Cates, J.J., et al., 2014. Anti-VEGF antibodies mitigate the development of radiation necrosis in mouse brain. Clin. Cancer Res. 20 (10), 2695–2702. https://doi.org/10.1158/1078-0432.CCR-13-1941.

Kamba, T., McDonald, D.M., 2007. Mechanisms of adverse effects of anti-VEGF therapy for cancer. Brit Jour Cancer 96, 1788–1795.

Kanis, J.A., WHO Study Group, 1994. Assessment of fracture risk and its application to screening for postmenopausal osteoporosis: synopsis of a WHO report. Osteo Int 4, 368–381.

Kanis, J.A., Melton, L.J., Christiansen, C., Johnston, C.C., Khalttaev, N., 1994. The diagnosis of osteoporosis. J Bone Min Res 9, 1137–1141.

King, R.J., Grant, P.J., 2016. Diabetes and cardiovascular disease: pathophysiology of a life-threatening epidemic. Herz 41 (3), 184–192. https://doi.org/10.1007/s00059-016-4414-8.

Lee, S., Bice, A., Hood, B., Ruiz, J., Kim, J., Prisby, R.D., 2018. Intermittent PTH improves the marrow microenvironment and endothelium-dependent vasodilation in bone arteries of aged rats. J Appl Physiol (1985) 124 (6), 1426–1437.

Li, Mosekilde, Sogaard, C.H., Danielsen, C.C., Torring, O., Nilsson, M.H.L., 1991. The anabolic effects of human parathyroid hormone (hPTH) on rat vertebral body mass are also reflected in the quality of bone, assessed by biomechanical testing: a comparison study between hPTH-(1-34) and hPTH-(1-84). Endocrinology 129, 421–428.

Liu, X., Tu, Y., Zhang, L., Qi, J., et al., 2014. Prolyl hydroxylase inhibitors protect from bone loss in OVX rats by increasing bone vascularity. Cell Biochem. Biophys. 69 (1), 141–149 May.

Lopez, A., Harada, K., Vasilakopoulou, M., Shanbhag, N., Ajani, J.A., 2019. Targeting angiogenesis in colorectal carcinoma. Drugs 79 (1), 63–74. https://doi.org/10.1007/s40265-018-1037-9.

Makowski, A.J., Uppuganti, S., Wadeer, S.A., Whitehead, J.M., et al., 2014. The loss of activating transcription factor 4 (ATF4) reduces bone toughness and fracture toughness. Bone 62, 1–9. https://doi.org/10.1016/j.bone.2014.01.021.

Manhard, M.K., Nyman, J.S., Does, M.D., 2017. Advances in imaging: approaches to fracture risk evaluation. Transl. Res. 181, 1–14. https://doi.org/10.1016/j.trsl.2016.09.006.

Maurea, N., Coppola, C., Piscopo, G., Galletta, F., et al., 2016. Pathophysiology of cardiotoxicity from target therapy and angiogenesis inhibitors. J Cardiovasc Med 17, e19–e26 Supp 1.

Mody, K., Baldeo, C., Bekaii-Saab, T., 2018. Anti-angiogenic therapy in colorectal cancer. Cancer J. 24 (4), 165–170. https://doi.org/10.1097/PPO.0000000000000328.

Mohan, G., Lay, E.Y., Berka, H., Ringwood, L., et al., 2017. A novel hybrid compound LLP2A-Ale both prevented and rescued the osteoporotic phenotype in a mouse model of GIOP. Calcif. Tissue Int. 100 (1), 67–79. https://doi.org/10.1007/s00223-016-0195-6.

Murakami, M., 2012. Signaling required for blood vessel maintenance: molecular basis and pathological manifestations. Intl Jour Vasc Medicine 293641. https://doi.org/10.1155/2012/293641.

Murakami, M., Simons, M., 2009. Regulation of vascular integrity. J. Mol. Med. 87, 571–582.

Nyman, J.S., Roy, A., Shen, X., Acuna, R.L., Tyler, J.H., Wang, X., 2006. The influence of water removal on the strength and toughness of cortical bone. J. Biomech. 39 (5), 931–938.

Nyman, J.S., Even, J.L., Jo, C.H., Herbert, E.G., Murry, M.R., Cockrell, G.E., et al., 2011a. Increasing duration of type 1 diabetes perturbs the strength-structure relationship and increases brittleness of bone. Bone 48, 733–740. https://doi.org/10.1016/j.bone.2010.12.016.

Nyman, J.S., Lynch, C.C., Perrien, D.S., Thiolloy, S., et al., 2011b. Differential effects between the loss of MMP-2 and MMP-9 on structural and tissue-level properties of bone. J Bone Min Res 26, 1252–1260. https://doi.org/10.1002/jbmr.326.

Ottoy, J., Verhaeghe, J., Niemantsverdriet, E., Wyffels, L., Somers, C., De Roeck, E., et al., 2017. Validation of the semi-quantitative static SUVR method for 18F-AV45 PET by pharmacokinetic modeling with an arterial input function. J. Nucl. Med. 58 (9), 1483. https://doi.org/10.2967/jnumed.116.184481.

Piert M, Zittel TT, Machulla HJ, Becker GA, Jahn M, Maier G, Bares R, Becker HD. Blood flow measurements with 15O-H2O and ^{18}F-fluoride ion PET in porcine vertebrae. J. Bone Miner. Res.. 1998; 13(8):1328–34.

Piert, M., Zittel, T.T., Becker, G.A., Jahn, M., Stahlschmidt, A., Maier, G., Machulla, H.J., Bares, R., 2001. Assessment of porcine bone metabolism by dynamic ^{18}F-fluoride ion PET: correlation with bone histomorphometry. J. Nucl. Med. 42 (7), 1091–1100.

Polly, B.J., Yuya, P.A., Akhter, M.P., Recker, R.R., Turner, J.A., 2012. Intrinsic material properties of trabecular bone by nanoindentation testing of biopsies taken from healthy women before and after menopause. Calcif. Tissue Int. 90 (4), 286–293. https://doi.org/10.1007/s00223-012-9575-8.

Prisby, R., Guignandon, A., Vandenbossche, A., Mac-Way, F., et al., 2011. Intermittent PTH is osteoanabolic but not osteoangiogenic and relocates bone marrow blood vessels closer to bone-forming sites. J. Bone Miner. Res. 26 (11), 2583–2596. https://doi.org/10.1002/jbmr.459.

Prisby, R., Menezes, T., Campbell, J., 2013. Vasodilation to PTH in bone arteries is dependent upon the vascular endothelium and is mediated partially via VEGF signaling. Bone 54 (1), 68–75. https://doi.org/10.1016/j.bone.2013.01.028.

Raouf, S., Bertelli, G., Ograbek, A., Field, P., Tran, I., 2018. Real-world use of bevacizumab in metastatic colorectal, metastatic breast, advanced ovarian and cervical cancer: a systematic literature review. Future Oncol. https://doi.org/10.2217/fon-2018-0480. Oct 31.

Rhee, Y., Park, S.Y., Kim, Y.M., Lee, S., Lim, S.K., 2009. Angiogenesis inhibitor attenuates PTH-induced anabolic effect. Biomed. Pharmacother. 63, 63–68.

Rizzo, S., Farlay, D., Akhter, M.P., Boskey, A., et al., 2018. Variables reflecting the mineralization of bone tissue from fracturing versus nonfracturing postmenopausal nonosteoporotic women. JBMR Plus 2 (6), 323–327. https://doi.org/10.1002/jbm4.10062.

Roschger, P., Misof, P.B., Paschalis, E., Fratzl, P., Klaushofer, K., 2014. Changes in the degree of mineralization with osteoporosis and its treatment. Curr Osteoporos Rep 12, 338–350. https://doi.org/10.1007/s11914-014-0218-z.

Ross, P.D., Genant, H.K., Davis, J.W., Miller, P.D., Wasnich, R.D., 1993. Predicting vertebral fracture incidence from prevalent fractures and bone density among non-black, osteoporotic women. Osteo Int 3, 120–126.

Rubin, M.R., 2017. Skeletal fragility in diabetes. Ann. N. Y. Acad. Sci. 1402 (1), 18–30. https://doi.org/10.1111/nyas.13463.

Saag, K.G., Zanchetta, J.R., Devogelaer, J.P., Adler, R.A., et al., 2009. Effects of teriparatide versus alendronate for treating GIOP: 36 month results of a randomized, double-blind, controlled trial. Arthritis Rheum. 60 (11), 3346–3355.

Schmidt, C., Priemel, M., Kohler, T., Weusten, A., et al., 2003. Precision and accuracy of peripheral quantitative computed tomography (pQCT) in the mouse skeleton compared with histology and microcomputed tomography (MicroCT). J. Bone Miner. Res. 18 (8), 1486–1496.

Sellmeyer, D.E., Civitelli, R., Hofbauer, L.C., Khosla, S., Lecka-Czernik, B., Schwartz, A.V., 2016. Skeletal metabolism, fracture risk, and fracture outcomes in Type 1 and Type 2 diabetes. Diabetes 65 (7), 1757–1766. https://doi.org/10.2337/db16-0063.

Senger, D.R., 2010. Vascular endothelial growth factor: much more than an angiogenesis factor. Mol. Biol. Cell 21, 377–379.

Soret, M., Bacharach, S.L., Buvat, I., 2007. Partial-volume effect in PET tumor imaging. J. Nucl. Med. 48 (6), 932–945.

Tabbaa, S.M., Horton, C.O., et al., 2014. Role of vascularity for successful bone formation and repair. Crit. Rev. Biomed. Eng. 42, 319–348.

Tegnebratt, T., Lu, L., Eksborg, S., Chireh, A., Damberg, P., et al., 2018. Treatment response assessment with (R)-[11C]PAQ PET in the MMTV-PyMT mouse model of breast cancer. EJNMMI Res. 8 (1), 25. https://doi.org/10.1186/s13550-018-0380-x.

Temmerman, O.P., Raijmakers, P.G., Heyligers, I.C., Comans, E.F., et al., 2008. Bone metabolism after total hip revision surgery with impacted grafting: evaluation using H2150 and [18F] fluoride PET; a pilot study. Mol. Imaging Biol. 10, 288–293.

Timmins, P.A., Wall, J.C., 1977. Bone water. Calcif. Tissue Res. 23, 1–5.

Turner, C.H., Burr, D.B., 1993. Basic biomechanical measurements of bone: a tutorial. Bone 14, 595–608.

Tyagi, N., Kandel, M., Munjal, C., Qipshidze, N., et al., 2011a. Homocysteine mediated decrease in bone blood flow and remodeling: role of folic acid. J. Orthop. Res. 29 (10), 1511–1516. https://doi.org/10.1002/jor.21415.

Tyagi, N., Vacek, T.P., Fleming, J.T., Vacek, J.C., Tyagi, S.C., 2011b. Hyperhomocysteinemia decreases bone blood flow. Vasc. Health Risk Manag. 25, 31–35. https://doi.org/10.2147/VHRM.S15844.

Van Staa, T.P., Laan, R.F., Barton, I.P., Cohen, S., Reid, D.M., Cooper, C., 2003. BMD threshold and other predictors of vertebral fracture in patients receiving oral glucocorticoid therapy. Arthritis Rheum. 48 (11), 3224–3229.

Weinstein, R.S., Wan, C., Liu, Q., Wang, Y., Almeida, M., et al., 2010. Endogenous glucocorticoids decrease skeletal angiogenesis, vascularity, hydration, and strength in aged mice. Aging Cell 9 (2), 147–161. https://doi.org/10.1111/j.1474-9726.2009.00545.

Wootton R, Doré C. The single-passage extraction of ^{18}F in rabbit bone. Clin. Phys. Physiol. Meas.. 1986; 7(4):333–43.

Wu, F., Tamhane, M., Morris, M.E., 2012. Pharmacokinetics, lymph node uptake, and mechanistic PK model of near-infrared dye-labeled bevacizumab after IV and SC administration in mice. AAPS J. 14 (2), 252–261. https://doi.org/10.1208/s12248-012-9342-9.

Zeb, A., Ali, S.R., Rohra, D.K., 2007. Mechanism underlying hypertension and proteinuria caused by bevacizumab. J. Coll. Physicians Surg. Pak. 17 (7), 448–449.